

SCIENTIFIC REPORTS



OPEN

Histological validation of fast macromolecular proton fraction mapping as a quantitative myelin imaging method in the cuprizone demyelination model

Received: 12 October 2016

Accepted: 24 March 2017

Published: 24 April 2017

Marina Yu Khodanovich¹, Irina V. Sorokina², Valentina Yu Glazacheva¹, Andrey E. Akulov^{1,3}, Nikolay M. Nemirovich-Danchenko¹, Alexander V. Romashchenko³, Tatyana G. Tolstikova², Lilia R. Mustafina⁴ & Vasily L. Yarnykh^{1,5}

Cuprizone-induced demyelination in mice is a frequently used model in preclinical multiple sclerosis research. A recent quantitative clinically-targeted MRI method, fast macromolecular proton fraction (MPF) mapping demonstrated a promise as a myelin biomarker in human and animal studies with a particular advantage of sensitivity to both white matter (WM) and gray matter (GM) demyelination. This study aimed to histologically validate the capability of MPF mapping to quantify myelin loss in brain tissues using the cuprizone demyelination model. Whole-brain MPF maps were obtained *in vivo* on an 11.7T animal MRI scanner from 7 cuprizone-treated and 7 control C57BL/6 mice using the fast single-point synthetic-reference method. Brain sections were histologically stained with Luxol Fast Blue (LFB) for myelin quantification. Significant ($p < 0.05$) demyelination in cuprizone-treated animals was found according to both LFB staining and MPF in all anatomical structures (corpus callosum, anterior commissure, internal capsule, thalamus, caudoputamen, and cortex). MPF strongly correlated with quantitative histology in all animals ($r = 0.95$, $p < 0.001$) as well as in treatment and control groups taken separately ($r = 0.96$, $p = 0.002$ and $r = 0.93$, $p = 0.007$, respectively). Close agreement between histological myelin staining and MPF suggests that fast MPF mapping enables robust and accurate quantitative assessment of demyelination in both WM and GM.

Macromolecular proton fraction (MPF) is a biophysical parameter defined within the two-pool model of magnetization transfer (MT)¹ that describes the amount of macromolecular protons characterized by solid-like nuclear magnetic resonance (NMR) spin dynamics and involved into magnetization exchange with free water protons in biological systems. During past decade, MPF has attracted remarkable attention as a quantitative biomarker of myelin due to high sensitivity to demyelination and strong correlations between MPF and myelin content in neural tissues reported in a number of studies^{2–12}. Associations between MPF and myelination were established in a variety of models and objects including excised demyelinated peripheral nerve², postmortem multiple sclerosis (MS) brain³, rat experimental autoimmune encephalomyelitis⁴, shiverer mouse^{5,6}, lipopolysaccharide-induced focal lesion in the rat brain⁷, shaking pup⁸, cuprizone-induced demyelination in mice^{9,10}, as well as normal rat brain¹¹ and spinal cord¹².

MPF or its associated quantity, pool size ratio (PSR) can be measured by a variety of quantitative MT (qMT) techniques based on semi-selective perturbation of either macromolecular or water proton populations¹³. Common approaches allowing reconstruction of MPF maps from magnetic resonance imaging (MRI) data

¹Research Institute of Biology and Biophysics, Tomsk State University, Tomsk, Russian Federation. ²Institute of Organic Chemistry, Siberian Branch of the Russian Academy of Sciences, Novosibirsk, Russian Federation. ³Institute of Cytology and Genetics, Siberian Branch of the Russian Academy of Sciences, Novosibirsk, Russian Federation. ⁴Siberian State Medical University, Tomsk, Russian Federation. ⁵Department of Radiology, University of Washington, Seattle, WA, United States. Correspondence and requests for materials should be addressed to V.L.Y. (email: yarnykh@uw.edu)

include Z-spectroscopic imaging based on the analysis of signal dependence on the offset frequency and power of an off-resonance saturation pulse^{14,15} and on-resonance techniques based on the analysis of bi-exponential longitudinal relaxation^{16,17}. These methods allow measurements of several parameters of the two-pool model including MPF and require collection of multiple image sets that results in time-consuming data acquisition rendering them inapplicable in clinics. An alternative fast method allowing whole-brain MPF mapping based on a single MT-weighted image, reference image, and a T_1 map was recently proposed¹⁸. This technique was tested in multiple sclerosis (MS)¹⁹ and mild traumatic brain injury²⁰ studies and demonstrated a promise as a robust clinically-targeted myelin imaging approach. In the above clinical studies, the fast single-point MPF mapping method¹⁸ demonstrated the capability to detect subtle microscopic demyelination in normal-appearing brain tissues including both white matter (WM) and gray matter (GM) and revealed the primary clinical relevance of cortical GM demyelination in MS¹⁹. Time efficiency of single-point MPF mapping has been further improved based on the recent synthetic-reference image reconstruction algorithm^{21,22}, which requires only three source images and enables generation of three-dimensional (3D) MPF maps with high spatial resolution, whole-brain coverage, and clinically acceptable scan time. While the fast single-point MPF mapping method based on either synthetic^{21,22} or actually acquired¹⁸ reference image showed highly consistent MPF measurements with the standard Z-spectroscopic method in both human¹⁸ and animal²² brain *in vivo*, this approach is still lacking direct histological validation as a quantitative myelin imaging modality.

Cuprizone-induced demyelination in mice is a widely used model of MS that reproduces certain pathological aspects of the disease, such as depletion of oligodendrocytes, myelin degradation, microglial activation, and astrogliosis accompanied with inflammation, hydrocephalus, and brain atrophy^{23–26}. Cuprizone administration typically results in global demyelination of WM and GM with a variable extent across anatomical structures and without formation of macroscopic focal lesions^{23–26}. This feature makes the cuprizone model a very suitable tool for evaluation and validation of quantitative imaging methods intended to measure microscopic demyelination in normal-appearing brain tissues. The overall goal of this study was to validate the fast synthetic-reference MPF mapping method using quantitative histology in the murine cuprizone demyelination model.

Results

Comparison between groups. Example MPF maps and LFB stained sections of control and cuprizone-treated murine brains are presented in Fig. 1. MPF maps of control animals demonstrated excellent tissue contrast between WM and GM and clear delineation of anatomical structures. Cuprizone-treated mice had visually reduced tissue contrast on MPF maps, especially in the corpus callosum and a slight overall reduction of the image intensity that can be appreciated when compared to control maps presented in the same absolute scale (Fig. 1). A visible reduction in the optical density on LFB stained brain sections of mice treated with cuprizone also can be appreciated in both WM and GM structures (Fig. 1). Quantitative comparison of MPF values and LFB optical densities in a series of anatomical regions between cuprizone-treated and control animals is presented in Table 1. Both MPF and LFB staining intensity in all WM and GM anatomical structures demonstrated a statistically significant decrease in the cuprizone group. Figure 2 compares the effect sizes characterizing group differences across anatomical structures. According to both MPF and LFB data, the largest effect of demyelination was found in the corpus callosum. Despite smaller relative changes in MPF, MPF mapping and LFB staining demonstrated a comparable performance in discriminating cuprizone-treated animals from the control group in terms of the effect size due to smaller variability of MPF measurements.

Correlations between MPF and histology. Results of linear regression analyses of MPF values as a function of LFB optical density for individual and averaged across anatomical structures data are presented in Table 2, and corresponding plots are shown in Fig. 3. In the pooled sample including data for each anatomical structure in each animal at each location from bregma, MPF values and LFB optical densities were strongly correlated ($r = 0.88$, $p < 0.001$) (Fig. 3a). This correlation became even stronger ($r = 0.95$, $p < 0.001$) after averaging data across animals for each structure (Fig. 3b). Regression analyses for separate groups of cuprizone-treated and control animals demonstrated remarkably similar results in terms of correlation strengths and coefficients of regression equations (Table 2). Particularly, for the subsamples of individual animals and structures, correlation coefficients were $r = 0.88$ ($p < 0.001$) for the cuprizone group and $r = 0.87$ ($p < 0.001$) for the control group. No significant differences between groups were found for correlation coefficients ($p = 0.78$) and slopes ($p = 0.80$) and intercepts ($p = 0.79$) of the regression lines. Very strong correlations were also observed for average structure data in both groups ($r = 0.96$, $p = 0.002$ for cuprizone-treated animals and $r = 0.93$, $p = 0.007$ for control animals) with no significant differences in regression coefficients ($p = 0.58$ for slopes and 0.56 for intercepts) and correlation strengths ($p = 0.72$).

Regional distinctions in the corpus callosum demyelination. The extent of demyelination in the corpus callosum was evaluated additionally in the rostral-caudal and medial-lateral directions. The results of the analysis of variance (ANOVA) for different regions of the corpus callosum are presented in Fig. 4. The patterns of the cuprizone treatment effect on regional MPF values and LFB optical density appeared substantially similar (Fig. 4). The significant main effect of treatment was observed for both MPF ($F = 39.67$, $p < 0.001$) and LFB optical density ($F = 13.76$, $p = 0.006$) measurements in all regions (Fig. 4). In the medial-lateral direction, no significant main effect of the region ($F = 0.18$, $p = 0.68$ for MPF and $F = 0.03$, $p = 0.86$ for LFB optical density) was observed, but significant interactions between the effects of treatment and region were found for both MPF ($F = 12.26$, $p = 0.004$) and LFB ($F = 13.76$, $p = 0.006$) data. In the rostral-caudal direction, the significant main effect of the region was identified for both MPF ($F = 144.37$, $p < 0.001$) and LFB ($F = 7.64$, $p < 0.02$), while interactions between the effects of treatment and region did not reach statistical significance ($F = 1.74$, $p = 0.21$).

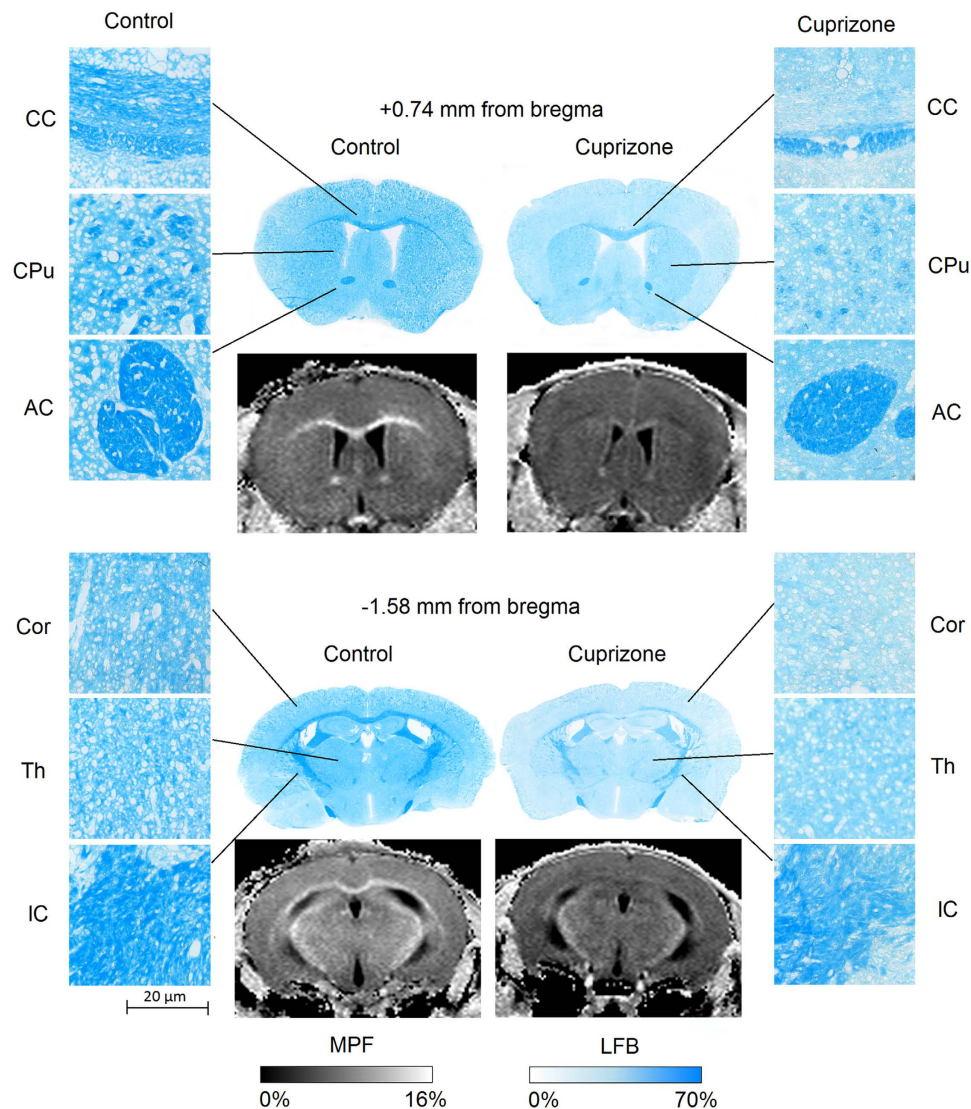


Figure 1. Example coronal brain LFB stained histological sections and cross-sections of 3D MPF maps of the control (left) and cuprizone-treated (right) mice taken through the caudoputamen (+0.74 mm from bregma, top) and thalamus (−1.58 mm from bregma, bottom). Magnified views illustrate normal tissue appearance (left column) and demyelination (right column) on LFB stained sections in the corpus callosum (CC), anterior commissure (AC), internal capsule (IC), caudoputamen (CPu), thalamus (Th), and cerebral cortex (Cor). MPF maps are presented with the grayscale range corresponding to 0–16%. The scale of LFB optical densities corresponds to the range of 0–70%.

for MPF and $F = 2.84$, $p = 0.13$ for LFB). Interactions between factors of the rostral-caudal and medial-lateral direction were also insignificant ($F = 0.96$, $p = 0.35$ for MPF and $F = 0.03$, $p = 0.87$ for LFB).

Scan-rescan repeatability of MPF mapping. Bland–Altman plots for repeated MPF measurements in a series of anatomic structures obtained from two consecutive MRI scans are presented in Fig. 5. Detailed report of the statistical analysis of repeatability is provided as a Supplementary Material (Supplementary Table S1). MPF values in all anatomic structures demonstrated close agreement with no significant bias between two measurements ($p > 0.1$ for all structures) and equal variances within each measurement ($p > 0.1$ for all structures). Within-subject coefficients of variation (CoV) for specific structures were as follows: 1.2% for the corpus callosum, 4.9% for the anterior commissure, 1.8% for the internal capsule, 1.0% for the thalamus, 1.9% for the caudoputamen, and 1.9% for the cortex.

Discussion

The key finding of this study is very close agreement between MPF measured by the fast single-point method and quantitative histology in both normal and demyelinated mouse brain across a range of WM and GM anatomical structures. This agreement is confirmed by both strong correlations between MPF and histology and comparable effect sizes for detecting demyelination in both WM and GM. Fast MPF mapping and LFB staining in the corpus

Parameter	MANOVA	Structure	Control (mean \pm SD)	Cuprizone (mean \pm SD)	p
MPF (%)	Wilks' Lambda = 0.047, F = 23.35, p < 0.001	Corpus callosum	13.15 \pm 0.73	9.65 \pm 0.95	<0.001
		Anterior commissure	11.93 \pm 0.74	10.78 \pm 0.77	0.014
		Internal capsule	12.74 \pm 0.67	11.75 \pm 0.69	0.018
		Thalamus	10.01 \pm 0.44	9.41 \pm 0.51	0.035
		Caudate putamen	8.54 \pm 0.25	8.10 \pm 0.33	0.016
		Cortex	8.13 \pm 0.22	7.67 \pm 0.27	0.005
LFB OD (%)	Wilks' Lambda = 0.101, F = 10.40, p = 0.003	Corpus callosum	49.14 \pm 3.23	29.35 \pm 4.27	<0.001
		Anterior commissure	46.09 \pm 7.61	37.48 \pm 4.01	0.021
		Internal capsule	52.54 \pm 8.43	39.92 \pm 5.87	0.007
		Thalamus	25.76 \pm 3.69	20.59 \pm 4.90	0.046
		Caudate putamen	30.68 \pm 6.21	18.64 \pm 5.09	0.002
		Cortex	16.46 \pm 3.40	12.21 \pm 3.30	0.035

Table 1. Mean values and standard deviations of MPF and LFB optical densities in the brain anatomical structures of control (n = 7) and cuprizone-treated (n = 7) mice. Abbreviations: MANOVA, multivariate analysis of variance; SD, standard deviation; MPF, macromolecular proton fraction; LFB, luxol fast blue; OD, optical density.

Animal data	Sample	r	r ²	n	p	Slope (95% CI), p	Intercept (95% CI), p
Individual	Pooled	0.882	0.779	112	<0.001	0.124 (0.112, 0.137), <0.001	6.278 (5.860, 6.670), <0.001
	Control	0.866	0.750	56	<0.001	0.121 (0.105, 0.145), <0.001	6.243 (5.476, 7.009), <0.001
	Cuprizone	0.879	0.772	56	<0.001	0.125 (0.104, 0.139), <0.001	6.300 (5.751, 6.986), <0.001
Structure-averaged	Pooled	0.947	0.897	12	<0.001	0.135 (0.102, 0.167), <0.001	5.941 (4.854, 7.027), <0.001
	Control	0.932	0.870	6	0.007	0.139 (0.099, 0.178), 0.007	5.650 (2.736, 8.564), 0.006
	Cuprizone	0.962	0.927	6	0.002	0.135 (0.083, 0.188), 0.002	5.996 (4.513, 7.480), <0.001

Table 2. Linear regression analysis of associations between MPF values and LFB optical densities. Abbreviation: CI, confidence interval.

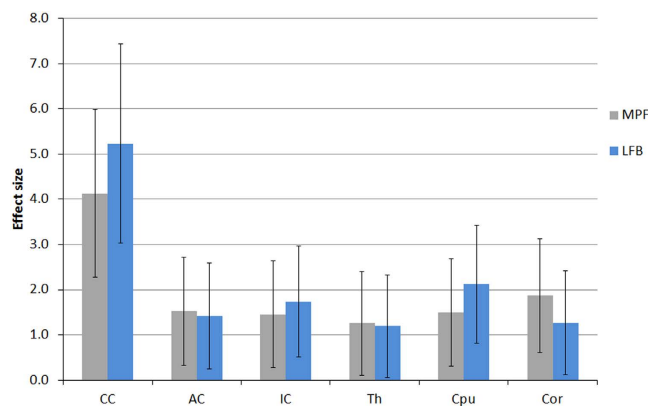


Figure 2. Effect sizes (Cohen's d) corresponding to group differences in mean MPF and LFB optical densities between control and cuprizone-treated mice for the following brain anatomic structures: corpus callosum (CC), anterior commissure (AC), internal capsule (IC), thalamus (Th), caudoputamen (CPu), and cerebral cortex (Cor). Error bars represent 95% confidence intervals.

callosum also demonstrated very similar capability to measure regional variations in demyelination within a single anatomic structure. The results of this study corroborate earlier reports of strong correlations between MPF and LFB optical density in the normal rodent brain¹¹ and the capability of MPF to detect cuprizone-induced demyelination not only in WM but also in cortical GM⁹. Of particular note, the strengths of correlations between MPF and LFB staining across WM and GM structures reported in this study appeared essentially similar to the data for the normal rat brain¹¹, as the correlation coefficients larger than 0.9 were found in both studies. It should be emphasized that the patterns and strengths of correlations between MPF and LFB staining discovered in this study were nearly identical for the groups of control and cuprizone-treated animals. This finding suggests that demyelination provides the primary pathological substrate of an MPF decrease in the cuprizone model,

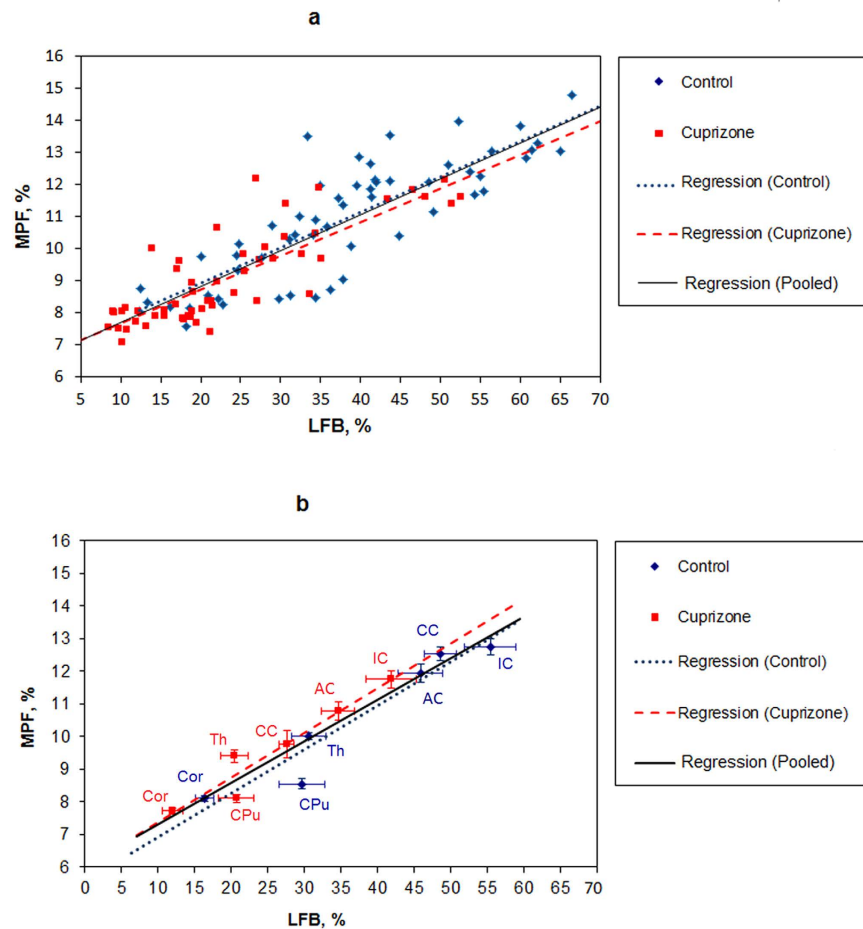


Figure 3. Linear regressions of MPF values on myelin density according to LFB staining in anatomical structures of the murine brain for individual measurements in each animal and structure (a) and mean values in each structure (b). Blue and red dots correspond to control and cuprizone-treated animals, respectively. Black lines depict the plots of the regression equations for the pooled datasets including both groups. Blue and red lines represent the separate regression plots for the control and cuprizone-treated groups, respectively. Error bars in the panel (b) represent standard errors of mean MPF and LFB optical densities in anatomical structures. Anatomical structures are labeled as follows: corpus callosum (CC), anterior commissure (AC), internal capsule (IC), thalamus (Th), caudoputamen (CPu), and cerebral cortex (Cor).

whereas potential influences on MPF of other factors that might affect various quantitative MRI measurements (such as inflammation and gliosis) are minor, if not negligible. While not fully generalizable to MPF changes in focal MS lesions in humans due to a possible confounding effect of edema, this conclusion provides a uniform conceptual framework for the interpretation of MPF as a biomarker of demyelination in normal appearing brain tissues. A recent study¹⁹ have identified a significant decrease of MPF in normal-appearing WM and GM in MS and close associations between MPF in normal-appearing brain tissues and clinical status. Furthermore, MPF changes in normal appearing brain tissues demonstrated a much higher clinical relevance than MPF in lesions or lesion volume¹⁹. In accordance with a commonly accepted view of MS as a whole-brain disease²⁷, the development and validation of sensitive and specific quantitative biomarkers of visually undetectable demyelination in normal-appearing brain tissues may bring both studies of new therapies and individual clinical care in MS to a principally new level. Taken together with earlier pre-clinical and clinical observations^{9,11,19,20}, the results of this study suggest that MPF provides a robust quantitative measure of the myelin content in both WM and GM, while the technical simplicity, short scan time, and whole-brain coverage enabled by the single-point synthetic-reference MPF mapping method^{21,22} make MPF a sensible biomarker for a variety of pre-clinical and clinical studies.

Cuprizone-induced demyelination of WM in mice has been studied by a variety of MRI methods^{9,10,28–42}. A vast majority of these studies were primarily focused on the corpus callosum, the site of most prominent myelin loss^{23–26}, which can be easily detected by routine T_2 - and T_1 -weighted imaging^{28–31} and a number of quantitative techniques including diffusion tensor imaging (DTI)^{9,29,32–39}, conventional MT ratio (MTR) imaging^{9,28,34,36,40–42}, qMT^{9,10}, and multi-component relaxation analysis³⁸. Several MRI studies also investigated demyelination in other WM structures, such as cerebral peduncles³², anterior commissure³², optic tracts³², external capsule^{9,10,30,32}, and cingulum^{30,32} which are affected by cuprizone intoxication to a lesser extent^{32,43}. Of note, demyelination of the

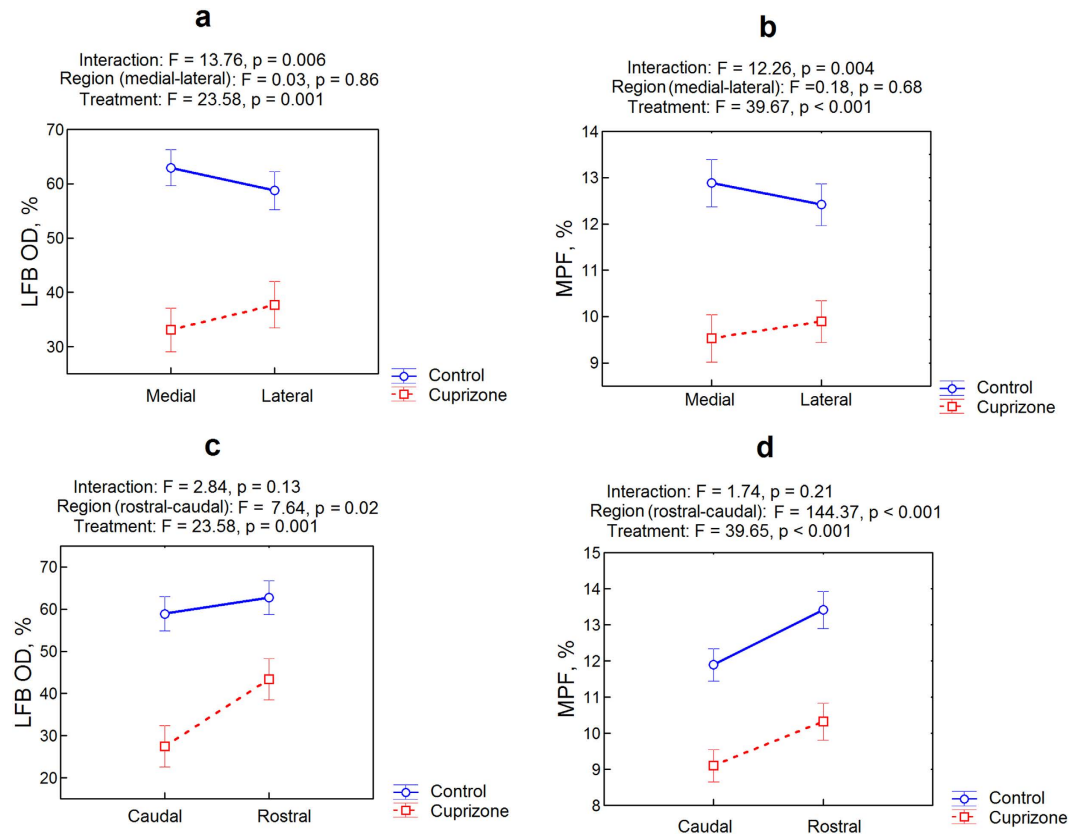


Figure 4. Regional distinctions in the corpus callosum demyelination according to ANOVA based on LFB optical density (a,c) and MPF (b,d) measurements. Plots (a) and (b) represent the effect of medial-to-lateral direction. Plots (c) and (d) represent the effect of caudal-to-rostral direction. Blue and red colors correspond to the control and cuprizone-treated groups, respectively. Error bars represent standard errors.

corpus callosum in the cuprizone model exhibits substantial spatial and temporal variability^{29,39,42–46}. Both MPF mapping and histology in our study confirmed the presence of the medial-to-lateral gradient of demyelination that is in agreement with the earlier publication⁴². However, in contrast to previous studies^{29,39,42–46}, we did not find significant distinctions in the myelin loss in the rostral-caudal direction. The most probable explanation of this discrepancy is a substantially longer cuprizone treatment period (8 weeks) in our study compared to earlier ones where the rostral-caudal gradient of demyelination was detected after 4–6 weeks of cuprizone administration^{29,39,42–46}. As such, regional distinction in the myelin content observable within a certain time frame might have been equalized due to either more extensive demyelination or concurrent remyelination^{23,39,46}. In agreement with this explanation, a reduction of rostral-caudal differences in demyelination was observed during prolonged cuprizone treatment (up to 12 weeks)³⁹. Another possible reason is inherent spatial variations of the myelin content in the normal corpus callosum as indicated by both MPF mapping and LFB staining (Fig. 4), which might mask relatively subtle regional differences in the demyelination. While spatial patterns of cuprizone-induced demyelination generally have a complex dependence on the treatment dose, duration, and mouse strain^{29,39,42–46}, our study indicates that MPF provides nearly identical to histology results in quantifying a variable extent of myelin loss in WM.

Cortical and subcortical GM demyelination is a characteristic feature of the cuprizone model according to histological studies^{47–51}, though MRI data about GM in cuprizone-treated animals are scarce. Particularly, a decrease of MTR was reported in deep GM⁴¹, while MTR could not distinguish cortical demyelination between treatment and control groups^{9,34,41}. A quantitative parameter based on multicomponent T_2 relaxation, myelin water fraction^{52,53}, which has been proposed as a myelin biomarker, was unable to detect both cortical and subcortical GM demyelination, while showing a significant effect in the corpus callosum and cerebellar WM in a recent cuprizone murine *ex vivo* study³⁸. Quantitative indexes derived from DTI data, such as fractional anisotropy and radial diffusivity were sensitive to cuprizone-induced changes in WM^{9,29,32–38} but failed to identify distinctions in GM^{9,37}. A more sophisticated diffusion-based technique, diffusion kurtosis imaging (DKI) demonstrated quantitative changes in the cortex of cuprizone-treated mice³⁷. However, these changes appeared inconsistent with changes in the corpus callosum, thus suggesting a complex mechanism determining a behavior of DKI parameters that cannot be reduced to demyelination alone³⁷. Significant cortical changes in cuprizone-treated mice were reported for MPF, cross-relaxation rate constant, and T_1 based on the analysis of Z-spectroscopic qMT data⁹. To the best of our knowledge, none of previous cuprizone model studies quantitatively compared any MRI technique with histology in the context of absolute myelin content measurements across a range of anatomical structures including

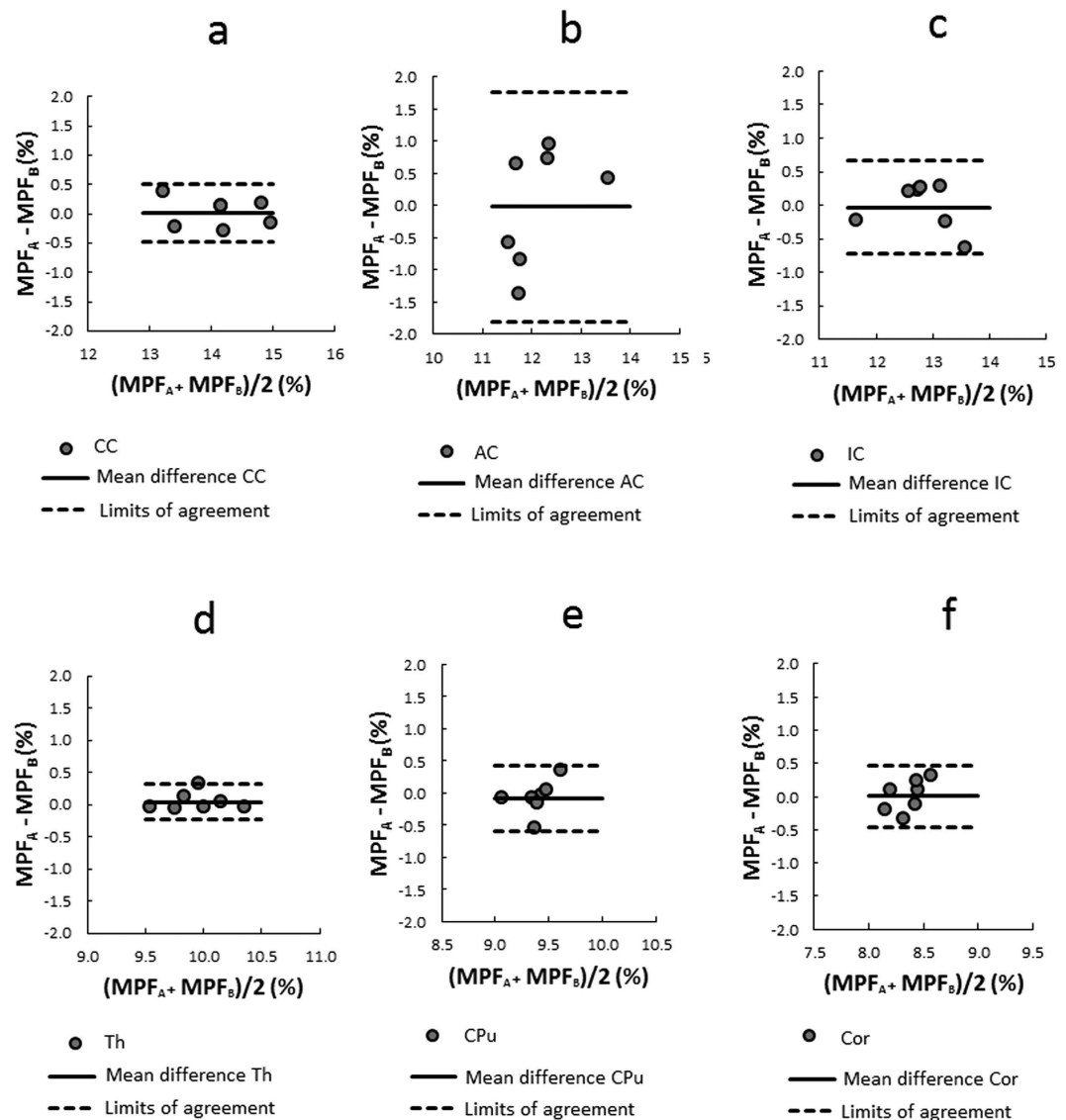


Figure 5. Bland–Altman plots comparing mean MPF values between two consecutive measurements in the following anatomical structures: corpus callosum (a), anterior commissure (b), internal capsule (c), thalamus (d), caudoputamen (e), and cerebral cortex (f). Solid and dashed lines correspond to the mean difference and limits of agreement, respectively.

WM and both cortical and subcortical GM. This study demonstrates that MPF measurements based on the fast single-point synthetic-reference method^{21,22} provide a similar to quantitative histology performance in the assessment of both WM and GM demyelination. A number of post-mortem histological studies have indicated a considerable amount of cortical and subcortical GM demyelination in MS in addition to WM damage^{27,54–57}. High clinical relevance of cortical demyelination in MS has been established in a recent study¹⁹, where MPF in cortical GM was found to be the strongest predictor of disability and the secondary progressive MS disease phenotype¹⁹. As such, the histologically validated capability of fast MPF mapping to accurately quantify GM demyelination makes this method especially attractive from the clinical standpoint.

Another useful feature of fast MPF mapping in the context of both pre-clinical and clinical studies is high reliability of results. Our study of scan-rescan repeatability has demonstrated excellent performance of the method in both WM and GM structures. For MPF measurements in all explored anatomical structures, except for the anterior commissure, within-subject CoV did not exceed 2%. The MPF values in the anterior commissure had a higher variability with CoV of about 5% that is probably due to the small size and associated partial volume effect for this structure. Repeatability of fast MPF mapping in the murine brain approaches earlier data for the human brain⁵⁸ where within-subject CoV of 1.5 and 1.1% were reported for WM and GM, respectively⁵⁸. Slightly larger CoV in the present work can be addressed to the manual procedure of image analysis as opposed to global brain tissue segmentation in the human study⁵⁸. At the same time, both this and previous⁵⁸ studies indicate that the effect of instrumental factors on variability of MPF measurements is minimal.

Compared to other quantitative MRI techniques proposed for myelin characterization, fast MPF mapping offers several practical advantages. An empirical value describing the MT effect, MTR has been widely used to characterize demyelination⁵⁹. While sensitivity of MTR to myelin mainly originates from its dependence on MPF^{11,15,19}, MTR also depends on T_1 . MPF and T_1 contribute into MTR in opposite directions, thus reducing its sensitivity to myelin content variations^{15,19}. Additionally, the dependence on T_1 makes MTR sensitive to the magnetic field strength and the effect of paramagnetic ions, such as iron, which frequently confounds demyelination, particularly in subcortical GM^{57,60,61}. MPF itself is independent of the presence of paramagnetic substances and field strength²². Alternative semi-empirical indexes describing the MT effect, such as MT saturation⁶², and MTR difference observed in the recent inhomogeneous MT experimental method⁶³ were proposed to overcome limitations of MTR. While the maps of the above quantities provide similar to MPF brain tissue contrast, these techniques have not been histologically validated, and the feasibility of their use for absolute quantitation at different field strengths remains uncertain. In contrast to DTI parameters associated with myelination (fractional anisotropy and radial diffusivity)^{32–34}, MPF is insensitive to directional properties and spatial organization of WM fiber tracts, which inevitably confound DTI-based measurements and result in high anatomical heterogeneity of corresponding indices that is unrelated to the myelin content^{64–66}. In contrast to relaxation-based methods aimed to extract myelin water fraction from multi-component T_2 ⁵², T_2^* ⁶⁷, or combined T_1 and T_2 data analysis⁵³, MPF is insensitive to errors caused by iron deposition^{21,68} and variability of relaxation times associated with magnetic field strength²². MPF also has been shown to provide a more accurate measure of myelin than multi-component T_2 , since the latter is subjected to systematic errors caused by inter-compartmental water exchange¹². A new relaxation-based method, relaxation along a fictitious field (RAFF) has recently emerged and showed a promise for myelin quantitation based on the comparisons with histology⁶⁹. However, it remains unclear at this point, whether quantitative data obtained with this approach depend on magnetic field and paramagnetic contributions and whether a RAFF mapping technique can provide sufficient time efficiency and image quality for clinical applications. Finally, MPF maps obtained by the fast single-point synthetic-reference method^{21,22} offer a substantially better spatial resolution and image quality *in vivo* than parametric maps typically available within DTI, multi-component relaxation, and multi-parameter qMT methods.

Conclusions

Fast 3D MPF mapping provides a robust clinically-targeted quantitative myelin imaging modality that showed the capability to detect demyelination in normal-appearing brain tissues in recent MS and mild traumatic brain injury studies. This study provides the first quantitative histological validation of the fast MPF mapping method in the animal demyelination model. Very strong correlations between histological myelin staining and MPF suggest that the method enables accurate quantitative assessment of the myelin content in both WM and GM and that demyelination is a major or even sole pathological substrate of MPF changes in demyelinating diseases.

Methods

Animal procedures and histological processing. All animal experiments were performed in accordance with the rules adopted by the European Convention for the Protection of Vertebrate Animals used for Experimental and other Scientific Purposes. The experimental protocol was approved by the Bioethical Committee of the Institute of Cytology and Genetics of the Siberian Branch of the Russian Academy of Sciences and the Bioethical Committee of the Biological Institute at the Tomsk State University. Fourteen five-week-old C57BL/6 male mice were obtained from the vivarium of the N.N.Vorozhtzov Institute of Organic Chemistry (Novosibirsk, Russian Federation). Animals were housed with a 12 hours dark-light cycle at the temperature of $21 \pm 2^\circ\text{C}$, and humidity of $40 \pm 2\%$. Food and water were provided *ad libitum*. Seven mice were treated 0.3% cuprizone solution in drinking water during 8 weeks to induce demyelination, and seven control mice received regular vivarium chow and water. Imaging was performed under isoflurane anesthesia (1.5–2% in oxygen) with respiratory monitoring during the scan.

After scanning, mice were transcardially perfused with 4% paraformaldehyde (PFA) under ether anesthesia. The brains were removed and fixed overnight in PFA at 4°C . Then the brains were cryoprotected in graded concentration of sucrose in phosphate buffer (24 h at 10% and 24 h at 20%) at 4°C , frozen in liquid nitrogen, and stored at -80°C . Coronal brain sections with $10\ \mu\text{m}$ thickness were prepared using an HM525 cryostat (Thermo Fisher Scientific, Walldorf, Germany). Histological myelin staining was performed using Luxol Fast Blue (LFB) colorant (Bio-Optica, Milano, Italy). Whole-brain sections were photographed using an Axio Imager Z2 microscope (Carl Zeiss AG, Göttingen, Germany) with the EC PlanNeofluar $1\times/0.025$ objective and AxioVision 4.8 software. Identical imaging parameters (voltage of microscope lamp and exposure time) were set for all photographed slices.

Additional seven eight-week-old C57BL/6 male mice were used to assess scan-rescan repeatability of MPF mapping. Animals were kept under standard vivarium conditions, as specified above, and scanned twice with one week interval between scans.

MRI acquisition and processing. Mice were imaged on an 11.7 Tesla horizontal-bore animal MRI scanner (BioSpec 117/16 USR; Bruker BioSpin, Ettlingen, Germany) with manufacturer's four-channel mouse brain surface coil. Imaging was performed under isoflurane anesthesia (1.5–2% in oxygen) with respiratory monitoring during the scan. A fast high-resolution 3D MPF mapping protocol was implemented according to the previously described single-point method with synthetic reference image normalization^{21,22}, and scan parameters were adapted for mouse whole-brain imaging. The protocol included the following sequences applied in the coronal plane with 3D field-of-view of $20 \times 20 \times 24\ \text{mm}$:

- (1) MT-weighted spoiled gradient echo (GRE) imaging: repetition time (TR) = 22 ms, echo time (TE) = 2.5 ms, flip angle (FA) = 9°, spectral bandwidth (BW) = 125 kHz, off-resonance saturation by the Gaussian pulse with offset frequency of 4.5 kHz, effective FA = 90°, and duration of 10 ms, 3D matrix 200 × 200 × 48, spatial resolution 100 × 100 × 500 μm³, four signal acquisitions, scan time 10 min 34 s;
- (2) T₁-weighted spoiled GRE imaging: TR = 16 ms, TE = 2.5 ms, FA = 16°, BW = 125 kHz, 3D matrix 200 × 200 × 48, spatial resolution 100 × 100 × 500 μm³, four signal acquisitions, scan time 7 min 41 s;
- (3) Proton-density (PD)-weighted spoiled GRE imaging: TR = 16 ms, TE = 2.5 ms, FA = 3°, BW = 125 kHz, 3D matrix 200 × 200 × 48, spatial resolution 100 × 100 × 500 μm³, four signal acquisitions, scan time 7 min 41 s;
- (4) B₀ mapping based on the dual-TE GRE phase-difference method⁷⁰: TR = 20 ms, TE₁ = 2.4 ms, TE₂ = 4.1 ms, FA = 8°, BW = 200 kHz, 3D matrix 100 × 100 × 48, spatial resolution 200 × 200 × 500 μm³, one signal acquisition, scan time 1 min 36 s.
- (5) B₁ mapping based on the dual-TR actual flip-angle imaging (AFI) method⁷¹: TR₁ = 13 ms, TR₂ = 65 ms, TE = 3.7 ms, FA = 60°, BW = 59.5 kHz, 3D matrix 100 × 100 × 48, spatial resolution 200 × 200 × 500 μm³, one signal acquisition, scan time 4 min 45 s.

The GRE and AFI sequences were implemented with optimal radiofrequency and gradient spoiling based on the excitation pulse phase increments of 169° for GRE and 39° for AFI⁷². In all sequences, linear phase-encoding order with fractional (75%) *k*-space acquisition in the slab selection direction was used. The total protocol execution time was about 35 min.

Reconstruction of MPF maps was carried out using custom-written C-language software based on the algorithm detailed elsewhere²¹. In brief, this algorithm computes MPF maps from three source images (MT-, T₁-, and PD-weighted) with correction of B₀ and B₁ field non-uniformities by voxel-based iterative single-point solution of the matrix pulsed MT equation¹⁸ with a calculated synthetic reference image for data normalization²¹.

The same protocol and map reconstruction was implemented to examine reproducibility of MPF mapping.

Image analysis. MPF maps and microphotographs of LFB stained histological sections were analyzed using publicly available ImageJ software (National Institutes of Health, Bethesda, MD, USA). Two brain locations (−1.58 mm and +0.74 mm from bregma) defined according to a mouse brain atlas⁷³ were chosen for quantitative analysis. MPF values and LFB optical densities were measured for a series of WM and GM structures including corpus callosum, anterior commissure, internal capsule, thalamus, caudoputamen, and cortex. Regions-of-interest (ROIs) of a standard size and shape were manually placed on MPF maps and photographs of LFB stained sections within investigated brain structures using a mouse brain atlas⁷³ as reference. The scheme of ROI measurements is exemplified in Fig. 6. MPF values for each anatomical structure were quantified by averaging ROI measurements obtained from 3D MPF maps corresponding to each location from bregma. Myelin densities on LFB stained photographs were quantified using the procedure modified from that described by Underhill, *et al.*¹¹. The mean intensity of the red channel (*I_R*) in a ROI was measured from RGB images as a quantity characterizing the complementary blue channel saturation. Specifically, visual perception of a more saturated blue color reflects stronger light absorption in the red region of the spectrum associated with stained myelin that translates into a lower intensity of the red channel in RGB images. Additionally, the mean intensity of the red channel in the background was measured on each photograph in four ROIs outside the brain. The intensities from the four above ROIs were averaged and used as the background correction factor (*I_B*). LFB optical density (in %) was subsequently calculated for each ROI as 100 × [1 − (*I_R*/*I_B*)], which yields a higher myelin content for increasing values. Individual ROI measurements were obtained from three adjacent sections per each location from bregma and averaged for each anatomical structure.

Statistical analysis. All statistical analyses were carried out in Statistica 10.0 for Windows (StatSoft Inc, Tulsa, OK, USA). Mean values and standard deviations (SD) of MPF and LFB optical density were calculated for each anatomical structure. Normality of the data within animal groups and residuals in regression analyses was assessed using Shapiro-Wilk test. No significant deviations from the normal distribution were found, and therefore, parametric analyses were used. MPF values and quantitative histology data were compared between cuprizone-treated and control animals using one-way multivariate analysis of variance (MANOVA) followed by independent-samples t-tests for individual anatomical structures. Distinctions in variables between animal groups were described by the effect size (Cohen's *d*) calculated as the ratio of the mean difference to the pooled standard deviation.

Pearson's correlation coefficient (*r*) and linear regression analysis were used to determine associations between MPF values and LFB optical densities across anatomical structures and animals. Significance of differences between Pearson's correlation coefficients for the two groups of animals was tested using Fisher's *r*-to-*z* transformation. Slopes and intercepts of regression equations were compared between groups using analysis of covariance (ANCOVA)⁷⁴ where MPF values were used as a dependent variable, LFB optical density was used as a covariate, and group membership (control or cuprizone-treated) was used as a categorical factor.

Regional distinctions in the corpus callosum demyelination were assessed using three-way analysis of variance (ANOVA) with the factors of treatment, ROI location in the rostral-caudal direction, and ROI location in the medial-lateral direction. The model included the main effects of factors and their pairwise interactions.

An agreement between MPF maps obtained from two repeated scans was assessed using Bland–Altman plots for each anatomical structure. Significance of the bias between repeated MPF measurements was examined using the one sample t-test for the mean difference. The limits of agreement were calculated as the mean difference ± 1.96 SD of the mean difference. To estimate variability between repeated measurements, the within-subject coefficients of variation was calculated as the percentage ratio of SD to the mean of paired measurements. The

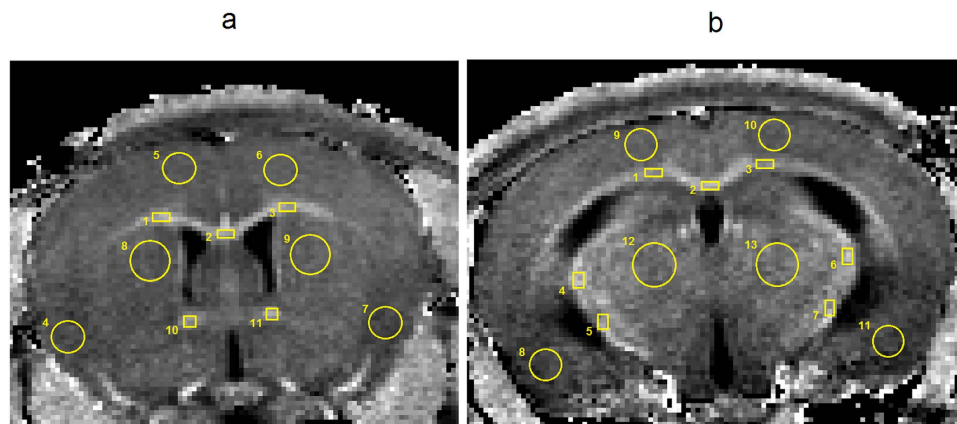


Figure 6. Representative cross-sections of a 3D MPF map of a control mouse taken at two locations from bregma with the superimposed sets of ROIs within investigated WM and GM brain structures. (a) Location at +0.74 mm from bregma with ROI numbers corresponding to the following structures: 1, 2, 3 - corpus callosum; 4, 5, 6, 7 - cerebral cortex; 8, 9 - caudoputamen; 10, 11 - anterior commissure. (b) Location at -1.58 mm from bregma with ROI numbers corresponding to the following structures: 1, 2, 3 - corpus callosum; 4, 5, 6, 7 - internal capsule; 8, 9, 10, 11 - cerebral cortex; 12, 13 - thalamus.

Levene's test was used to assess equality of variances. Two-tailed tests were used in all analyses. Statistical significance was defined as a p value less than 0.05.

References

- Henkelman, R. M. *et al.* Quantitative interpretation of magnetization transfer. *Magn. Reson. Med.* **29**, 759–766 (1993).
- Odrobina, E. E., Lam, T. Y., Pun, T., Midha, R. & Stanisz, G. J. MR properties of excised neural tissue following experimentally induced demyelination. *NMR Biomed.* **18**, 277–284 (2005).
- Schmierer, K. *et al.* Quantitative magnetization transfer imaging in postmortem multiple sclerosis brain. *J. Magn. Reson. Imaging* **26**, 41–51 (2007).
- Rausch, M. *et al.* Characterization of white matter damage in animal models of multiple sclerosis by magnetization transfer ratio and quantitative mapping of the apparent bound proton fraction. *Mult. Scler.* **15**, 16–27 (2009).
- Ou, X., Sun, S. W., Liang, H. F., Song, S. K. & Gochberg, D. F. The MT pool size ratio and the DTI radial diffusivity may reflect the myelination in shiverer and control mice. *NMR Biomed.* **22**, 480–487 (2009).
- Ou, X., Sun, S. W., Liang, H. F., Song, S. K. & Gochberg, D. F. Quantitative magnetization transfer measured pool-size ratio reflects optic nerve myelin content in *ex vivo* mice. *Magn. Reson. Med.* **61**, 364–371 (2009).
- Janve, V. A. *et al.* The radial diffusivity and magnetization transfer pool size ratio are sensitive markers for demyelination in a rat model of type III multiple sclerosis (MS) lesions. *Neuroimage* **74**, 298–305 (2013).
- Samsonov, A. *et al.* Quantitative MR imaging of two-pool magnetization transfer model parameters in myelin mutant shaking pup. *Neuroimage* **62**, 1390–1398 (2012).
- Thiessen, J. D. *et al.* Quantitative MRI and ultrastructural examination of the cuprizone mouse model of demyelination. *NMR Biomed.* **26**, 1562–1581 (2013).
- Turati, L. *et al.* *In vivo* quantitative magnetization transfer imaging correlates with histology during de- and remyelination in cuprizone-treated mice. *NMR Biomed.* **28**, 327–337 (2015).
- Underhill, H. R., Rostomily, R. C., Mikheev, A. M., Yuan, C. & Yarnykh, V. L. Fast bound pool fraction imaging of the *in vivo* rat brain: Association with myelin content and validation in the C6 glioma model. *Neuroimage* **54**, 2052–2065 (2011).
- Dula, A. N., Gochberg, D. F., Valentine, H. L., Valentine, W. M. & Does, M. D. Multiexponential T2, magnetization transfer, and quantitative histology in white matter tracts of rat spinal cord. *Magn. Reson. Med.* **63**, 902–909 (2010).
- Yarnykh, V. Mathematical modeling of the magnetization transfer effect in tissues. *J. Phys.: Conf. Ser.* **677**, 012001, 10.1088/1742-6596/677/1/012001 (2016).
- Sled, J. G. & Pike, G. B. Quantitative imaging of magnetization transfer exchange and relaxation properties *in vivo* using MRI. *Magn. Reson. Med.* **46**, 923–931 (2001).
- Yarnykh, V. L. Pulsed Z-spectroscopic imaging of cross-relaxation parameters in tissues for human MRI: theory and clinical applications. *Magn. Reson. Med.* **47**, 929–939 (2002).
- Gochberg, D. F., Kennan, R. P., Robson, M. D. & Gore, J. C. Quantitative imaging of magnetization transfer using multiple selective pulses. *Magn. Reson. Med.* **41**, 1065–1072 (1999).
- Gochberg, D. F. & Gore, J. C. Quantitative magnetization transfer imaging via selective inversion recovery with short repetition times. *Magn. Reson. Med.* **57**, 437–441 (2007).
- Yarnykh, V. L. Fast macromolecular proton fraction mapping from a single off-resonance magnetization transfer measurement. *Magn. Reson. Med.* **68**, 166–178 (2012).
- Yarnykh, V. L. *et al.* Fast whole-brain three-dimensional macromolecular proton fraction mapping in multiple sclerosis. *Radiology* **274**, 210–220 (2015).
- Petrie, E. C. *et al.* Neuroimaging, behavioral, and psychological sequelae of repetitive combined blast/impact mild traumatic brain injury in Iraq and Afghanistan war veterans. *J. Neurotrauma* **31**, 425–436 (2014).
- Yarnykh, V. L. Time-efficient, high-resolution, whole brain three-dimensional macromolecular proton fraction mapping. *Magn. Reson. Med.* **75**, 2100–2106 (2016).
- Naumova, A. V., Akulov, A. E., Khodanovich, M., Yu. & Yarnykh, V. L. High-resolution three-dimensional macromolecular proton fraction mapping for quantitative neuroanatomical imaging of the rodent brain in ultra-high magnetic fields. *Neuroimage* **147**, 985–993 (2017).
- Matsushima, G. K. & Morell, P. The neurotoxicant, cuprizone, as a model to study demyelination and remyelination in the central nervous system. *Brain Pathol.* **11**, 107–116 (2001).

24. Torkildsen, O., Brunborg, L. A., Myhr, K. M. & Bo, L. The cuprizone model for demyelination. *Acta Neurol. Scand. Suppl.* **188**, 72–76 (2008).
25. Acs, P. & Kalman, B. Pathogenesis of multiple sclerosis: what can we learn from the cuprizone model. *Methods Mol. Biol.* **900**, 403–431 (2012).
26. Kipp, M., Clarner, T., Dang, J. & Beyer, C. The cuprizone animal model: new insights into an old story. *Acta Neuropathol.* **118**, 723–736 (2009).
27. Lassmann, H., Brück, W. & Lucchinetti, C. F. The immunopathology of multiple sclerosis: an overview. *Brain Pathol.* **17**, 210–218 (2007).
28. Merkler, D. *et al.* Multicontrast MRI of remyelination in the central nervous system. *NMR Biomed.* **18**, 395–403 (2005).
29. Wu, Q. Z. *et al.* MRI identification of the rostral-caudal pattern of pathology within the corpus callosum in the cuprizone mouse model. *J. Magn. Reson. Imaging* **27**, 446–453 (2008).
30. Chandran, P. *et al.* Magnetic resonance imaging and histological evidence for the blockade of cuprizone-induced demyelination in C57BL/6 mice. *Neuroscience* **202**, 446–453 (2012).
31. Torkildsen, O. *et al.* Effects of dietary intervention on MRI activity, de- and remyelination in the cuprizone model for demyelination. *Exp. Neurol.* **215**, 160–166 (2009).
32. Song, S. K. *et al.* Demyelination increases radial diffusivity in corpus callosum of mouse brain. *Neuroimage* **26**, 132–140 (2005).
33. Sun, S. W. *et al.* Noninvasive detection of cuprizone induced axonal damage and demyelination in the mouse corpus callosum. *Magn. Reson. Med.* **55**, 302–308 (2006).
34. Zang, J. *et al.* *In vivo* and *ex vivo* diffusion tensor imaging of cuprizone-induced demyelination in the mouse corpus callosum. *Magn. Reson. Med.* **67**, 750–759 (2012).
35. Falangola, M. F. *et al.* Histological correlation of diffusional kurtosis and white matter modeling metrics in cuprizone-induced corpus callosum demyelination. *NMR Biomed.* **27**, 948–957 (2014).
36. Jelescu, I. O. *et al.* *In vivo* quantification of demyelination and recovery using compartment-specific diffusion MRI metrics validated by electron microscopy. *Neuroimage* **132**, 104–114 (2016).
37. Guglielmetti, C. *et al.* Diffusion kurtosis imaging probes cortical alterations and white matter pathology following cuprizone induced demyelination and spontaneous remyelination. *Neuroimage* **125**, 363–377 (2016).
38. Wood, T. C. *et al.* Whole-brain *ex-vivo* quantitative MRI of the cuprizone mouse. *PeerJ Preprints* **4**, e2323v1, 10.7287/peerj.preprints.2323v1 (2016).
39. Xie, M. *et al.* Rostrocaudal analysis of corpus callosum demyelination and axon damage across disease stages refines diffusion tensor imaging correlations with pathological features. *J. Neuropathol. Exp. Neurol.* **69**, 704–716 (2010).
40. Zaaraoui, W. *et al.* Monitoring demyelination and remyelination by magnetization transfer imaging in the mouse brain at 9.4 T. *MAGMA* **21**, 357–362 (2008).
41. Fjaer, S. *et al.* Deep Gray Matter Demyelination Detected by Magnetization Transfer Ratio in the Cuprizone Model. *PLoS One* **8**, e84162, 10.1371/journal.pone.0084162 (2013).
42. Tagge, I. *et al.* Spatio-temporal patterns of demyelination and remyelination in the cuprizone mouse model. *PLoS One* **11**, e0152480, 10.1371/journal.pone.0152480 (2016).
43. Yang, H. J. *et al.* Region-specific susceptibilities to cuprizone-induced lesions in the mouse forebrain: implications for the pathophysiology of schizophrenia. *Brain Res.* **1270**, 121–130 (2009).
44. Stidworthy, M. F., Genoud, S., Suter, U., Mantei, N. & Franklin, R. J. Quantifying the early stages of remyelination following cuprizone-induced demyelination. *Brain Pathol.* **13**, 329–339 (2003).
45. Binder, M. D. *et al.* Gas6 deficiency increases oligodendrocyte loss and microglial activation in response to cuprizone-induced demyelination. *J. Neurosci.* **28**, 5195–5206 (2008).
46. Steelman, A. J., Thompson, J. P. & Li, J. Demyelination and remyelination in anatomically distinct regions of the corpus callosum following cuprizone intoxication. *Neurosci. Res.* **72**, 32–42 (2012).
47. Skripuletz, T. *et al.* Cortical demyelination is prominent in the murine cuprizone model and is strain-dependent. *Am. J. Pathol.* **172**, 1053–1061 (2008).
48. Gudi, V. *et al.* Regional differences between grey and white matter in cuprizone induced demyelination. *Brain Res.* **1283**, 127–138 (2009).
49. Koutsoudaki, P. N. *et al.* Demyelination of the hippocampus is prominent in the cuprizone model. *Neurosci. Lett.* **451**, 83–88 (2009).
50. Norkute, A. *et al.* Cuprizone Treatment Induces Demyelination and Astrocytosis in the Mouse Hippocampus. *J. Neurosci. Res.* **87**, 1343–1355 (2009).
51. Pott, F. *et al.* Cuprizone effect on myelination, astrogliosis and microglia attraction in the mouse basal ganglia. *Brain Res.* **1305**, 137–149 (2009).
52. Mackay, A. *et al.* *In vivo* visualization of myelin water in brain by magnetic resonance. *Magn. Reson. Med.* **31**, 673–677 (1994).
53. Deoni, S. C., Rutt, B. K., Arun, T., Pierpaoli, C. & Jones, D. K. Gleaning multicomponent T1 and T2 information from steady-state imaging data. *Magn. Reson. Med.* **60**, 1372–1387 (2008).
54. Kutzelnigg, A. *et al.* Cortical demyelination and diffuse white matter injury in multiple sclerosis. *Brain* **128**, 2705–2712 (2005).
55. Lucchinetti, C. F. *et al.* Inflammatory cortical demyelination in early multiple sclerosis. *N. Engl. J. Med.* **365**, 2188–2197 (2011).
56. Gilmore, C. P. *et al.* Regional variations in the extent and pattern of grey matter demyelination in multiple sclerosis: a comparison between the cerebral cortex, cerebellar cortex, deep grey matter nuclei and the spinal cord. *J. Neurol. Neurosurg. Psychiatry* **80**, 182–187 (2009).
57. Pirko, I., Lucchinetti, C. F., Sriram, S. & Bakshi, R. Gray matter involvement in multiple sclerosis. *Neurology* **68**, 634–642 (2007).
58. Yarnykh, V. L. Reproducibility of fast three-dimensional macromolecular proton fraction mapping of the human brain: global tissue characterization and volume measurements. In *Proceedings of the 24th Annual Meeting of ISMRM*, Singapore **332** (2016).
59. Ropele, S. & Fazekas, F. Magnetization transfer MR imaging in multiple sclerosis. *Neuroimaging Clin. N Am.* **19**, 27–36 (2009).
60. Bakshi, R. *et al.* T2 hypointensity in the deep gray matter of patients with multiple sclerosis: a quantitative magnetic resonance imaging study. *Arch. Neurol.* **59**, 62–68 (2002).
61. Raz, E. *et al.* Relationship between iron accumulation and white matter injury in multiple sclerosis: a case-control study. *J. Neurol.* **262**, 402–409 (2015).
62. Helms, G., Dathe, H., Kallenberg, K. & Dechent, P. High-resolution maps of magnetization transfer with inherent correction for RF inhomogeneity and T1 relaxation obtained from 3D FLASH MRI. *Magn. Reson. Med.* **60**, 1396–1407 (2008).
63. Varma, G., Duhamel, G., de Bazelaire, C. & Alsop, D. C. Magnetization transfer from inhomogeneously broadened lines: A potential marker for myelin. *Magn. Reson. Med.* **73**, 614–622 (2015).
64. Mädlér, B., Drabycz, S. A., Kolind, S. H., Whittall, K. P. & MacKay, A. L. Is diffusion anisotropy an accurate monitor of myelination? Correlation of multicomponent T2 relaxation and diffusion tensor anisotropy in human brain. *Magn. Reson. Imaging* **26**, 874–888 (2008).
65. Wheeler-Kingshott, C. A. & Cercignani, M. About “axial” and “radial” diffusivities. *Magn. Reson. Med.* **61**, 1255–1260 (2009).
66. Underhill, H. R., Yuan, C. & Yarnykh, V. L. Direct quantitative comparison between cross-relaxation imaging and diffusion tensor imaging of the human brain at 3.0 T. *Neuroimage* **47**, 1568–1578 (2009).
67. Hwang, D., Kim, D. H. & Du, Y. P. *In vivo* multi-slice mapping of myelin water content using T2* decay. *Neuroimage* **52**, 198–204 (2010).

68. Krutenkova, E. P. *et al.* Demyelination and iron accumulation in subcortical gray matter (GM) in multiple sclerosis (MS). *Ann. Neurol.* **78**, S65–S65 (2015).
69. Hakkarainen, H. *et al.* MRI relaxation in the presence of fictitious fields correlates with myelin content in normal rat brain. *Magn. Reson. Med.* **75**, 161–168 (2016).
70. Skinner, T. E. & Glover, G. H. An extended two-point Dixon algorithm for calculating separate water, fat, and B0 images. *Magn. Reson. Med.* **37**, 628–630 (1997).
71. Yarnykh, V. L. Actual flip-angle imaging in the pulsed steady state: a method for rapid three-dimensional mapping of the transmitted radiofrequency field. *Magn. Reson. Med.* **57**, 192–200 (2007).
72. Yarnykh, V. L. Optimal radiofrequency and gradient spoiling for improved accuracy of T1 and B1 measurements using fast steady-state techniques. *Magn. Reson. Med.* **63**, 1610–1626 (2010).
73. Paxinos, G. & Franklin, K. *The mouse brain in stereotactic coordinates* (2nd ed. Academic Press, London, 2001).
74. McDonald, J. H. *Handbook of Biological Statistics* (3rd ed. Sparky House Publishing, Baltimore, Maryland, 2014).

Acknowledgements

The authors acknowledge financial support from the Russian Science Foundation (project № 14-45-00040) for experimental studies, data analysis, and manuscript preparation and from the National Institutes of Health (grant R21EB016135) for software development. V.L.Y. received partial salary support from the National Multiple Sclerosis Society grant RG 4864A1/1. Animal procedures were carried out at the Center for Genetic Resources of Laboratory Animals at the Institute of Cytology and Genetics (Siberian Branch, Russian Academy of Sciences) operating under support of the Ministry of Education and Science projects RFMEFI61914X0005 and RFMEFI62114X0010.

Author Contributions

M.Y.K., I.V.S., and V.L.Y. designed the study. M.Y.K. performed statistical analysis and wrote the manuscript. I.V.S. and T.G.T. were responsible for the development of the animal model. A.E.A. and A.V.R. performed MRI studies. V.Y.G. performed image analysis. N.M.N.-D. and L.R.M. performed histological processing and staining. V.L.Y. developed an MRI protocol and image processing software and critically revised the manuscript. All authors reviewed and approved the final version of the manuscript.

Additional Information

Supplementary information accompanies this paper at <http://www.nature.com/srep>

Competing Interests: The authors declare no competing financial interests.

How to cite this article: Yu. Khodanovich, M. *et al.* Histological validation of fast macromolecular proton fraction mapping as a quantitative myelin imaging method in the cuprizone demyelination model. *Sci. Rep.* **7**, 46686; doi: 10.1038/srep46686 (2017).

Publisher's note: Springer Nature remains neutral with regard to jurisdictional claims in published maps and institutional affiliations.



This work is licensed under a Creative Commons Attribution 4.0 International License. The images or other third party material in this article are included in the article's Creative Commons license, unless indicated otherwise in the credit line; if the material is not included under the Creative Commons license, users will need to obtain permission from the license holder to reproduce the material. To view a copy of this license, visit <http://creativecommons.org/licenses/by/4.0/>

© The Author(s) 2017